

Article

CONvective–STRAtiform Identification Neural Network (CONSTRAINN) for the WIVERN mission

Federico Mustich¹ and Alessandro Battaglia^{1,2*}  and Francesco Manconi^{1*}  and Pavlos Kollias^{3,4*}  and Antonio Parodi^{5*} 

¹ DIATI, Politecnico di Torino, 10129 Turin, Italy

² Earth Observation Science Group, Department of Physics and Astronomy, University of Leicester, Leicester LE1 7RH, UK

³ School of Marine and Atmospheric Sciences, Stony Brook University, NY, USA

⁴ Department of Atmospheric and Oceanic Sciences, McGill University, Montreal, QC, Canada

⁵ CIMA Foundation, Savona, Italy

* Correspondence: alessandro.battaglia@polito.it

Received: 05 September 2025; Accepted: XXXXX

Abstract: The WIVERN mission promises to deliver the first global observations of the three-dimensional wind field and the associated cloud and precipitation structure in a wide range of atmospheric phenomena, including isolated thunderstorms, tropical cyclones, mid-latitude frontal systems, and polar lows. A critical element in the development of the mission’s wind products is the differentiation between stratiform and convective regions. Convective regions are defined as those where vertical wind velocities exceed 1 m/s. This work introduces CONSTRAINN, a family of U-Net based neural network models that utilise all of WIVERN observables—including vertical profiles of reflectivity and Doppler velocity, as well as brightness temperatures—to reconstruct convective wind activity within the Earth’s atmosphere. Results show that the retrieved convective/stratiform masks are well reconstructed with an equitable threat score exceeding 0.6. Ablation experiments further reveal that Doppler Velocity signals are the most informative for the reconstruction task. Source code, data, and trained checkpoints are available, open-source and open-weights, at <https://github.com/Anatr1/CONSTRAINN>.

Keywords: Convective/Stratiform separation; Doppler radar; U-Net;

1. Introduction

The WIVERN (WInd VELOCITY Radar Nephoscope) mission concept, one of the two candidate missions competing for selection as the Earth Explorer 11 mission within the European Space Agency’s FutureEO programme, promises to revolutionize the study of clouds, with its 800 km swath fast conically scanning 94 GHz Doppler radar at an incidence angle of about 42 degrees [1–3]. This configuration allows WIVERN to measure in-cloud winds at the native horizontal resolution of 1 km along track, with approximately 600 m vertical resolution. The WIVERN Doppler velocity measurements will provide information on the motion of the cloud and precipitation particles along the Line of Sight (LoS), i.e., the antenna boresight looking direction. Because WIVERN observes the atmosphere at a slant incidence angle, the Doppler signal represents a combination of both horizontal and vertical air motions, as well as the hydrometeors’ sedimentation velocity. In regions where vertical motions are negligible and the hydrometeor fall speed can be accurately estimated, it is possible to retrieve the horizontal wind component projected along the horizontal line of sight (V_{HLoS})—the mission’s flagship product. This information can be used, for example, in data assimilation systems to improve numerical weather prediction [4,5]. To derive this wind product, it is essential to distinguish between atmospheric regimes where the vertical velocity (w) can be considered negligible (defined

as $|w| \leq 1$ m/s), referred to as stratiform, and those where w is significant, known as convective. In stratiform regions, V_{HLoS} can be directly derived under the assumption that vertical motion is minimal. Conversely, in convective regions, if V_{HLoS} can be reconstructed from nearby stratiform regions, it may then be possible to estimate the vertical wind component. These unique in-cloud wind products will then further provide:

- Full vector wind estimates within clouds over parts of the 800 km swath, by combining the forward and backward radar looks, offering an unparalleled perspective on cloud dynamics [6,7].
- Insights into convective organisation and anvils morphology, by combining the LoS winds with radar reflectivity to derive convective mass fluxes and assess radiative impacts [3].
- Advanced understanding of the processes governing the formation, organisation, and intensification of mesoscale convective systems, tropical cyclones, and mid-latitude windstorms [8].

The convective/stratiform (C/S) classification is also of general interest for scientific purposes as stratiform and convective regimes differ in two fundamental ways:

1. Formation mechanisms: convective precipitation is associated with strong vertical motions and the growth of hydrometeors via coalescence and/or riming, whereas, stratiform precipitation occurs in regions with much weaker vertical motion, dominated by vapour deposition and aggregation.
2. The distinct microphysical processes associated with each regime result in differing diabatic heating structures, which, in turn, influence large-scale atmospheric circulation in different ways [9].

Over the past 30 years, many methodologies have been developed to separate convective and stratiform regimes. Drawing on data from missions such as TRMM, GPM, CloudSat, and EarthCARE (for details on atmospheric radars, see Battaglia *et al.* [10]), the scientific community has gained considerable experience in classifying deep hydrometeor layers as either stratiform or convective using only the reflectivity measured by spaceborne radars, typically through echo-object classification schemes. For low frequency radar (such as the Ku-band radar on board the TRMM and GPM observatories) the fundamental concept is that in stratiform conditions there is a smooth transition between the solid to the liquid phase occurring at the freezing level which is marked by a bright band in the radar reflectivity [11]. In contrast, convective profiles are characterized by high reflectivities often exceeding 50 dBZ and extend to altitudes above 10 km without any evidence of a transition region at the freezing level [12].

Radars with WIVERN adopted frequency (94 GHz) are subject to return signal saturation due to non-Rayleigh effects (a 94-GHz rarely detects echoes above +20 dBZ, [13,14], significant signal attenuation [15], and multiple scattering effects that can distort the signal [16]. Despite these challenges, several studies use the CloudSat CPR reflectivity profile features near the cloud top to identify convective cores [17,18]. The underlying rationale is that the overshooting of high radar reflectivities is an indicator of the larger-size particles pushed high up only possible with the presence of strong rising updrafts. A key limitation of the spaceborne C/S classifications proposed so far is that they are mainly based on vertical profiles of reflectivities. These approaches generally lack direct dynamical information such as Doppler velocities, and make limited use of the spatial texture of the reflectivity field.

In addition to spaceborne approaches, substantial efforts have been made to classify convective and stratiform (C/S) regions using ground-based radar observations. Early attempts relied on rule-based heuristics, using radar reflectivity thresholds and pattern recognition techniques. The Steiner–Houze–Yuter (SHY95) algorithm identifies convective cores based on peak reflectivity and local neighbourhood contrast [19], while later fuzzy-logic methods extend the idea to three-dimensional

volumes [20]. These methods are simple and fast but struggle with bright-band artifacts and varying radar geometry.

In recent years, supervised models have gradually replaced fine-tuned threshold methods. [21] trained a k -nearest-neighbour classifier on WSR-98D Doppler fields and achieved a 10–15% skill boost over SHY95. Neural networks are now massively used in connection to C/S classification from geostationary observations. For example, [22] built a convolutional neural network (CNN) that detects overshooting tops linked to severe convection and is able to discriminate between intense and ordinary convection. [23] showed that gradient-boosted trees fed with spectral visible and infrared data outperform traditional texture metrics for convective region detection.

For passive microwave observations, [24] showed that a suite of machine-learning models trained on GPM Microwave Imager (GMI) brightness temperatures can already separate convective, stratiform and mixed precipitation with 90–94% global accuracy, while [25] applied a Bayesian ResNet to GPM–GMI microwave brightness temperatures, achieving >90% accuracy in distinguishing convective and stratiform precipitation while also providing per-pixel uncertainty estimates, underscoring the value of data-driven approaches for precipitation-type retrievals.

The U-Net encoder–decoder backbone has become the de facto standard for pixel-level classification tasks. For example, Hoeller *et al.* [26] applied a vanilla U-Net to identify convective cold pools, while Han *et al.* [27] reported similar improvements when using a U-Net-based nowcasting model to forecast 30-minute radar precipitation. More recently, Zhang and He [28] proposed an ensemble of lightweight U-Nets for processing FY-4B geostationary satellite imagery, achieving inference latencies below 100 ms per frame while maintaining a probability of detection (POD) greater than 0.70.

Beyond convective/stratiform (C/S) discrimination, the U-Net architecture has been successfully adapted for a variety of geophysical classification tasks, including cloud typing, land-cover mapping, and severe weather prediction. For instance, the 1D-CloudNet, a one-dimensional nested U-Net, combines Himawari-8 radiance data with CloudSat-derived labels to classify nine cloud categories at nadir [29].

Hybrid encoder designs have also enhanced the accuracy of land-cover segmentation in multispectral imagery [30], while multi-feature fusion U-Nets have improved overall classification performance across diverse surface imaging scenes [31].

Remarkably, U-Net variants have even been applied to generate spatiotemporal tornado risk maps, by leveraging multivariate fields from numerical weather prediction (NWP) models [32].

This work aims to exploit recent advances in U-Net to develop a C/S classification algorithm specific to the WIVERN mission. The mission's conical scanning Doppler radar provides a 2D curtain of reflectivity and Doppler velocity data, as well as 1D collocated measurements of brightness temperatures. The methodologies usually applied to 2D horizontal texture fields are therefore now being applied to 2D slanted cuts through the atmosphere. The goal is to identify pixels that are convective, i.e. those with vertical velocities exceeding 1 m/s, with downdrafts and updrafts combined into a single probabilistic score.

2. Simulations of WIVERN observables

The WIVERN instrument with its conically scanning wide-swath radar (Fig. 1(a)) represents a major technological innovation, unifying three advanced satellite sensing capabilities into a single system: range-resolved Doppler velocity, reflectivity measurements, and passive microwave observations. These are integrated through a unique radar–radiometer concept, enabling co-located active and passive measurements to maximize scientific synergy.

During ESA Phase-0 and Phase-A studies an instrument simulator has been developed that simulates all three WIVERN observables from both atmospheric and surface targets based on successive refinements [2,33,34] of the backbone simulator proposed in [35]. In brief, the simulator takes output from cloud resolving models that provides 3D fields of winds, hydrometeors, temperature, water

vapor and translate them in 94 GHz stimuli (i.e. scattering properties such as 94 GHz extinction, scattering and backscattering coefficients, single scattering albedo and asymmetry parameters). Then, each scene is illuminated by the WIVERN antenna and scanning pattern for any given orbit. The radar observables are simulated accounting for the sampling rate, the sensitivity and the specific pulse scheme of the instrument (details in [2]).

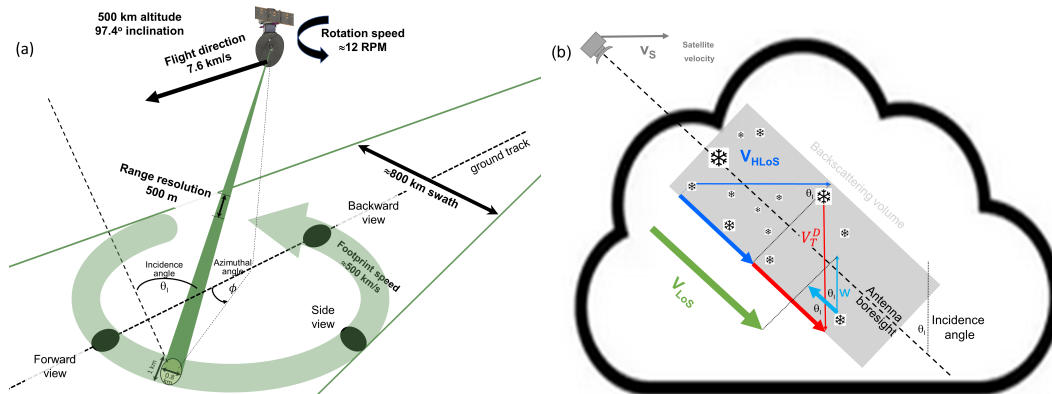


Figure 1. Panel (a): Conically scanning geometry envisaged for the WIVERN mission. The width of the footprint is exaggerated for illustration purposes. Panel (b): vector diagram explaining the WIVERN LoS equation showing how to relate V_{HLoS} , the vertical wind (w) and the Doppler terminal velocity (V_T^D) to the V_{LoS} measurement.

WIVERN most innovative measurement will be the LoS Doppler velocity (V_{LoS}). Because of the slant angle of observation this quantity will be affected by:

1. The Horizontal Line of Sight (HLoS) wind velocity (V_{HLoS}), i.e. the horizontal wind along the horizontally-projected LoS direction;
2. the vertical wind velocity, w ;
3. the radar reflectivity weighted terminal velocity of the hydrometeors (V_T^D) [36].

While the latter contribution can be generally estimated based on temperature and strength of the radar backscattered signal, the first two contributions are generally entangled. The WIVERN fundamental equation linking the Line-of-Sight (LoS) Doppler velocity (V_{LoS}) with the other three variables is given by

$$V_{LoS} = V_{HLoS} \sin(\theta_I) + \underbrace{(w + V_T^D)}_{V_z^D} \cos(\theta_I) \quad (1)$$

and is illustrated in Fig. 1b.

2.1. A dataset of tropical cyclone simulations

The training data used in this study were generated using the WIVERN end-to-end simulator. Simulations were driven by atmospheric conditions derived from a mesoscale numerical weather prediction system. Specifically, data from a WRF (Weather Research and Forecasting) model simulation of Hurricane Milton were used to create the dataset employed in this study. The WRF dataset spans the period from 6 October 2024 at 10:00 UTC to 8 October 2024 at 00:00 UTC, with output intervals of one hour (39 hours in total).

During this time, the cyclone evolved from a tropical storm to a Category 5 hurricane. Each hourly snapshot captures a domain of approximately $1250 \times 1250 \times 20 \text{ km}^3$ centred around the cyclone eye, with a horizontal resolution of roughly 1.5 km and vertical resolution of approximately 500 m (but finer at heights lower than 3 km). For each snapshot, 200-second simulations (equivalent to 40 full antenna rotations) were performed. The time domain was centred around the moment when the satellite's ground track passed closest to the hurricane eye. For each of the snapshots, overpasses were placed by

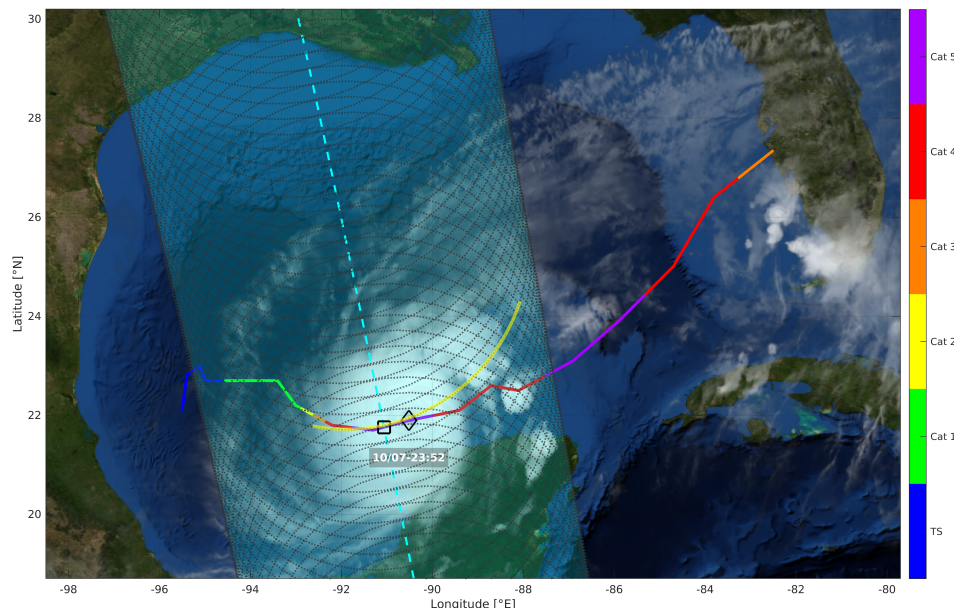


Figure 2. Representation of an overpass of WIVERN over hurricane Milton in the Gulf of Mexico for the 10/07 at 23:52 UTC. The track of hurricane Milton is shown, color coded to the intensity of the storm, from 5th October 2024 at 18:00 UTC to 10th October 2024 at 00:00 UTC. In white, cloud data was plotted using geostationary infrared data for the day of 8th October 2024 at 00:00 UTC. The square marker indicates the closest position of the satellite on the ground with respect to the cyclone eye (diamond marker). The cyan dashed line is the satellite ground track, while the gray dotted line represent the conical scan (the whole swath is highlighted by the shadowed region in cyan). The curtains for relevant quantities outputted by the simulator along the sector highlighted in yellow are plotted in Fig. 4.

translating an ascending ground track passing exactly over the eye from -6 to $+6$ deg in longitude in steps of 1 degree (13 tracks in total). Fig. 2 show a representation of the WIVERN sampling strategy in Hurricane Milton. The dataset was obtained by randomly running several combinations of the 13 possible tracks for each of the 39 hours of hurricane Milton data. The final dataset was produced by randomly selecting various combinations of these 13 tracks across the 39 time steps, yielding approximately 80 simulation runs in total. This approach ensured a rich diversity of atmospheric scenarios across a wide range of hurricane intensities.

From the simulation output, the key variables which compose the model inputs are extracted: vertical brightness temperature T_B^V (monodimensional), horizontal brightness temperature T_B^H (monodimensional), Doppler velocity V_{LoS} (2-dimensional), and reflectivity Z_m (2-dimensional), with a horizontal spacing of 1 km and a vertical spacing of roughly 70 m. In addition, the simulator outputs the “true” vertical component of the wind field, w_{LoS} , projected along the instrument LoS. To obtain the physical vertical velocity, w_{LoS} is divided by $\sin(42^\circ)$, reflecting the nominal incidence angle of the conically scanning beam (Fig. 1(a)).

An example of a simulated overpass is illustrated in Figs. 3, 4. Fig. 3 is a zoomed version that highlights the WIVERN dense sampling strategy. The Total Water Path (TWP) is indicative of areas with deep hydrometeor layers and the presence of vertically extended liquid water columns due to strong vertical air motions. Superimposed, the WIVERN scan, color-coded with the H channel brightness temperature T_B^H . In magenta, contours of actual convective regions are highlighted, where the maximum wind speed along the column exceeds 3 m/s.

Fig. 4 shows the three main radar products (Z_m , V_{LoS} and T_B) and corresponding relevant quantities (TWC, V_{HLoS} , and V_z^D) along a segment of the WIVERN slanted vertical cross section. In panels (a) and (b), the eye and eyewall of the hurricane are clearly identifiable at the centre of the plot. The eye is characterised by a column of clear air with near-zero wind velocity, while the

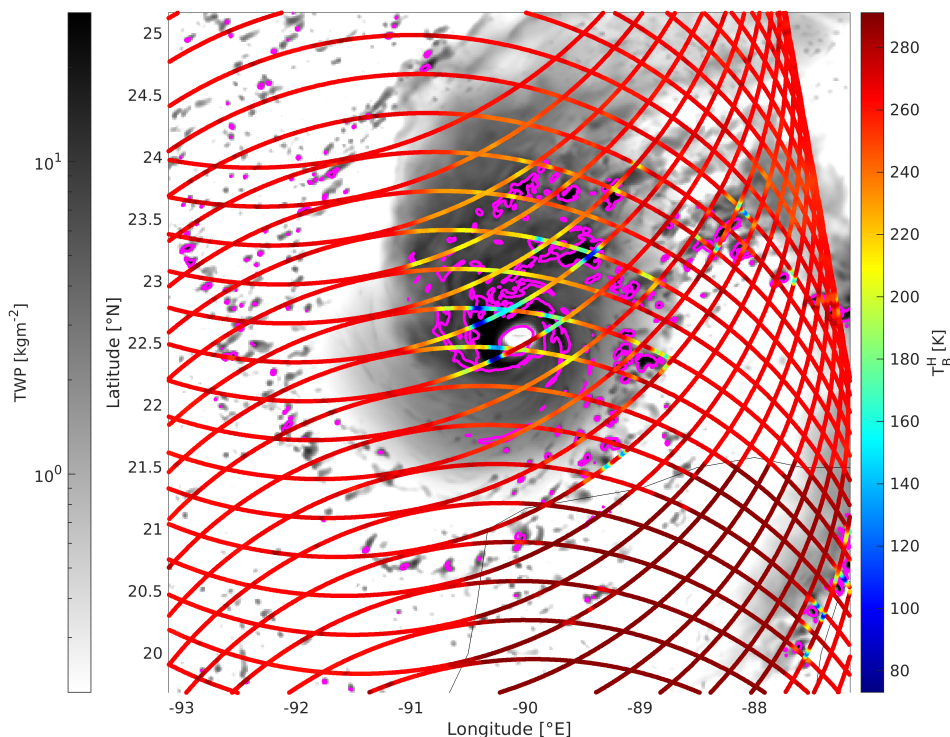


Figure 3. Detail of the simulated scan example, highlighting convective regions. In greyscale, the Total Water Path (TWP), i.e. the TWC integrated over the height. Superimposed, the WIVERN scan, color-coded with the H channel brightness temperature T_B^H . In magenta, contours of regions where the maximum of the windspeed in the column is over 3 m/s, which is the criterion used to identify convective cells.

surrounding eyewall is marked by high TWC, which leads to signal extinction in the Z_m field. Generally, Z_m correlates well with TWC: above the freezing level (approximately 5 km altitude), large anvil clouds containing high ice water content are visible, while rain bands with abundant low-level hydrometeors are evident at lower altitudes near the eyewall regions. Even within the eye, low clouds occasionally contribute to weak radar returns at lower levels.

Panels (c) and (d) show that the Doppler velocity signal is dominated by horizontal winds, displaying the characteristic dipole pattern of cyclonic circulation—winds of opposite sign appear on either side of the eye. In panel (f), convective vertical motions are apparent in the eyewall region, while below approximately 5 km, the vertical velocity is enhanced by precipitation fall speeds. Finally, Panel (e) reveals that highly convective regions are typically associated with lower brightness temperatures, consistent with deep, cold cloud tops.

In total, the dataset spans a distance of nearly 5.5×10^6 km along the satellite ground track. For storage and mini-batching purposes, the data curtain is divided into 10,912 non-overlapping segments, each covering 500 km along-track. All variables are stored in NetCDF4 format using 32-bit floating-point precision. Fig. 4 illustrates an example of a single chunk extracted from the full dataset.

Although the dataset, based on simulations of Hurricane Milton, provides a meteorologically rich test bed with prominent convective activity, convective regions remain a minority class within the full 5.5-million-kilometre dataset. Across the entire record, only 0.62% of the data corresponds to areas with vertical wind speeds exceeding 3 m/s, with an additional 3.67% falling within the range of 1–3 m/s. This reflects the well-documented sparsity of strong updraughts and downdraughts compared with widespread stratiform regions. The resulting class imbalance in the training labels is mitigated through loss reweighting and probability threshold tuning, as detailed in Sect. 3.

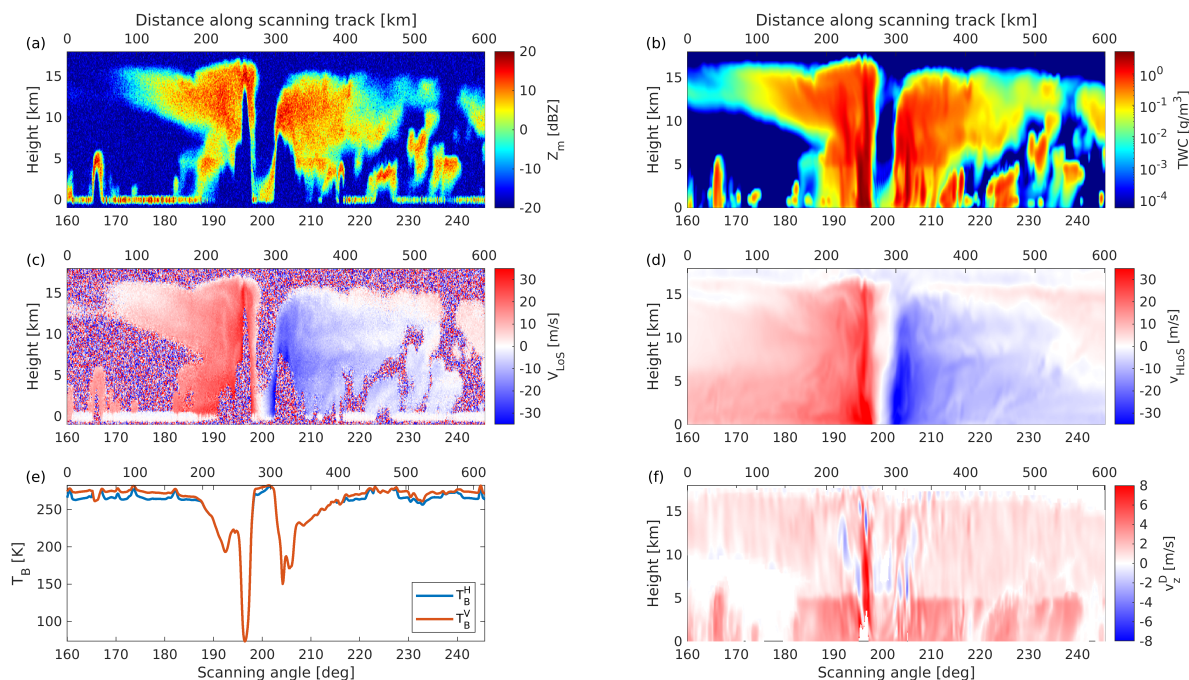


Figure 4. Curtains of the sector of the scan highlighted in yellow in Fig. 2. In the left column, from top to bottom, the observables: (a) measured reflectivity, (c) measured Doppler velocity, and (e) vertical and horizontal brightness temperature. In the right column, from top to bottom, the antenna weighted "true" quantities obtained directly from the WRF model: (b) Total Water Content (TWC), (d) horizontal component of the LoS wind, (f) vertical component of the LoS wind plus the hydrometeor terminal velocity.

3. Methodology

3.1. Link between WIVERN observables and convective identification

All three WIVERN observables (94 GHz reflectivities, line-of-sight Doppler velocities and 94 GHz brightness temperatures) contain valuable information related to the presence of convection. This statement is supported by insights gained from previous missions such as CloudSat and ongoing missions like EarthCARE, both of which employ cloud radars operating at the same frequency.

94 GHz Reflectivity Profile. Numerous studies have demonstrated that high radar reflectivity values near cloud tops observed by the CloudSat CPR (e.g. values exceeding 10 dBZ above 10 km altitude) are effective indicators of convective cores [17,18]. Within CloudSat data, three commonly applied criteria are used to identify deep convection:

1. The CPR cloud mask (2B-GEOPROF product) much exceed a value of 20.
2. There must be a continuous radar echo extending from below 2 km to above 10 km in altitude.
3. The echo-top height of the 10 dBZ reflectivity contour must exceed 10 km. A reflectivity of 10 dBZ is typically considered a proxy for the presence of precipitation-sized particles in convective clouds [37]. The extent to which such large particles are lifted towards the cloud top serves as an indirect measure of updraught intensity [38].

An example extracted from CloudSat data is shown in Fig. 5. The black dots indicate locations along the CPR data that meet the deep convection. The CPR profiles corresponding to two such profiles are shown in Panel (c) (dashed lines). There are distinct differences among these profiles with the blue line one having a clear signature of multiple scattering [16] with no evident transition between the solid and liquid phase at the melting layer and the cyan one, on the other hand, having a sharp transition at about 4 km with a large reflectivity gradient between 1 and 4 km, a signature of rain attenuation

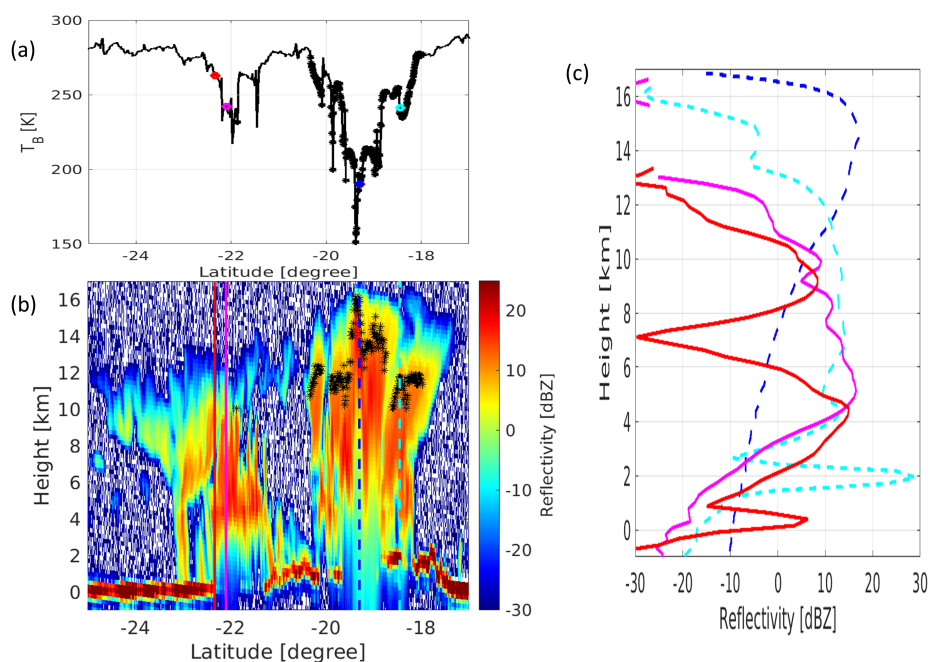


Figure 5. Precipitation event on the 11/01/2008 over Bolivia and Argentina observed in an ascending CloudSat overpass. (a) CloudSat 94-GHz T_b in K. (b) CPR reflectivity. (c) Example of CPR reflectivity profiles: two in deep convective cores meeting the criteria from Takahashi *et al.* [18] (dashed lines) and two in a stratiform region (continuous lines).

[39]. Profiles in more stratiform regions (red and magenta continuous lines) on the other hand, show a strong positive vertical gradient of reflectivity below the freezing level.

94 GHz Doppler Velocity. Observations from nadir-looking airborne radars (e.g. Heymsfield *et al.* [40]) and the recently launched EarthCARE mission [41] have revealed increased variability in vertical Doppler velocities in the presence of convective motions. In such environments, strong updraughts and downdraughts often occur in close proximity, resulting in significant spatial variability in the Doppler velocity measurements. The EarthCARE Doppler radar, which is nadir-pointing, provides direct measurements of the vertical Doppler velocity (V_z^D in Eq. 1). Recent findings by Galfione *et al.* [41] confirm that this variability is a reliable indicator of convective activity.

In contrast, WIVERN performs conical scanning at an incidence angle of 42° . Although the vertical component of the wind is attenuated by a factor of 0.74 due to the projection onto the line-of-sight (as described in Eq. 1), the LoS Doppler velocities from WIVERN will still be sensitive to the rapid fluctuations in vertical velocity (w) commonly found in convective regions.

94 GHz Brightness Temperature. Previous studies employing microwave radiometers have demonstrated that the presence of precipitation-sized ice particles leads to a depression in brightness temperatures (T_b) at higher frequencies (≥ 37 GHz), relative to the warmer background [42–44]. Among the various types of ice particles, graupel plays a key role in causing this depression at 94 GHz. Its presence in the atmospheric column is linked to the riming process, which is typically intensified by strong updraughts [45,46].

This characteristic is evident in CloudSat T_b observations: Panel (a) of Fig. 5 clearly shows a substantial drop in brightness temperature below 200 K in the vicinity of the convective core. While 94 GHz T_b measurements from CloudSat have been used to advance understanding of ice microphysics [47], it is surprising that they have not been widely exploited in studies of deep convection. Our simulations further support these findings, with T_b depressions reaching values below 100 K in intense convective cores.

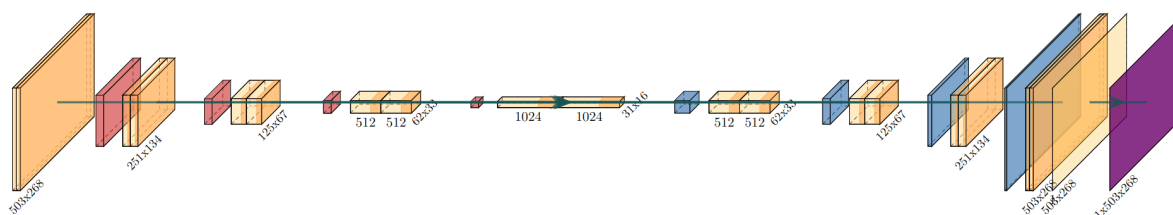


Figure 6. Network architecture for CONSTRAINN-medium. Numbers indicate each layer size. Orange: convolutional layers. Red: pooling layers. Blue: Unpooling layers. Purple: softmax layer.

Taken together, these results highlight the significant potential of all three WIVERN observables—94 GHz radar reflectivity, Doppler velocity, and brightness temperature—for convection identification. A distinct advantage in WIVERN’s case is that all three measurements are beam-matched, ensuring spatial and angular consistency in their retrievals.

3.2. Convective/Stratiform Mask

In our simulation framework, the first step involves estimating the WIVERN sampling volume-averaged vertical air motion. This is achieved by applying the antenna pattern weighting function to the modelled vertical velocities within the radar’s sampling volume. The resulting averaged vertical air motion serves as the reference truth for subsequent analysis.

Importantly, our models are not trained to reproduce the exact magnitude of the vertical velocity. Instead, the reference vertical velocity is first transformed into a smoothed convection–stratiform mask, which serves as the training target. The models are then trained to learn this classification structure rather than predict precise velocity values.

For each pixel-value w of the reference vertical velocity matrix, a corresponding target mask value m is obtained by mapping it to $[0, 1]$ with a linear rule:

$$m = \begin{cases} 0, & \text{if } |w| \leq 1 \text{ m/s} \\ 1, & \text{if } |w| \geq 3 \text{ m/s} \\ \frac{|w|-1}{2}, & \text{otherwise.} \end{cases} \quad (2)$$

Note that absolute values of w are considered, hence ignoring the vertical motion direction (i.e., no distinction between updrafts and downdrafts). m is set to NaN in regions which produce reflectivities below WIVERN sensitivity (-25 dBZ). The resulting mask is a floating-point values image whose values are between 0 and 1, whereas values close to 1 mark vigorous convection.

3.3. Pipeline Overview

Each 500 km segment of data is stored as an individual NetCDF file, which contains the four input channels—vertical and horizontal brightness temperatures, reflectivity, and Doppler velocity—along with the computed target mask.

To ensure consistency in data representation, the brightness temperature variables are tiled into 2D tensors, providing a common spatial shape across all input channels.

The dataset is divided into a training set and a cross-validation set using a 9:1 ratio. Reflectivity values below -25 dBZ are capped at -25 dBZ, and min–max normalisation is applied across all variables to standardise the input range for model training.

3.4. Network Architectures

Three encoder–decoder U-NET variants have been implemented. Details of their architectures are provided in Tab. 1. All models employ bilinear up-sampling, skip concatenations, a 1×1 output

Model Size	Parameters (M)	Initial Filters	Depth (down blocks)
Mini	8	32	4
Medium	30	64	5
Large	500	128	6

Table 1. Architectural summary of the three CONSTRAINNN variants. “Parameters” is the total number of trainable parameters (expressed in millions), “Initial Filters” is the number of feature maps in the first convolution, and “Depth” is the number of down-sampling (encoder) blocks.

convolution, and optional sigmoid activation for inference. Dropout is injected at the bottleneck to mitigate overfitting.

3.5. Training Setup

Overall, the training dataset consisted of 10912 samples, for a total of approximately 5.5 millions km and 45 GB of simulated track data. Utilizing a single NVIDIA A40 GPU, the duration for training spans from 3 to 4 hours for Mini configurations and extends up to 24 hours for Large setups.

3.6. Inference and evaluation

During evaluation the same cleaning and normalization steps are applied. The network is then executed in *sigmoid mode*: the raw logits from its final 1×1 convolution are passed through the sigmoid function

$$\sigma(z) = \frac{1}{1 + e^{-z}} \quad (3)$$

turning every pixel into a calibrated probability in the interval $[0, 1]$. Running the model in sigmoid mode produces true probabilities that can be directly compared with the continuous target mask or thresholded for ETS, POD, FAR and F_1 .

3.6.1. Metrics

For measuring performance, non-thresholded metrics were employed (Mean Absolute Error (MAE), Mean Squared Error (MSE) and Binary Cross Entropy Loss (BCE)), defined as:

$$\text{MAE} = \frac{1}{N} \sum_{i=1}^N |\hat{y}_i - y_i| \quad (4)$$

$$\text{MSE} = \frac{1}{N} \sum_{i=1}^N (\hat{y}_i - y_i)^2 \quad (5)$$

$$\text{BCE} = -\frac{1}{N} \sum_{i=1}^N y_i \ln \hat{y}_i + (1 - y_i) \ln(1 - \hat{y}_i) \quad (6)$$

where N is the number of valid pixels in each image, $\hat{y}_i \in [0, 1]$ is the network output and $y_i \in [0, 1]$ the target mask.

For further performance assessment our task is reformulated as a binary classification problem and four thresholded metrics are computed: Probability of Detection (POD), False Alarm Rate (FAR), Equitable Threats Score (ETS), F1-score.

$$\text{POD} = \frac{\text{TP}}{\text{TP} + \text{FN}} \quad (7)$$

$$\text{FAR} = \frac{\text{FP}}{\text{TP} + \text{FP}} \quad (8)$$

$$\text{ETS} = \frac{\text{TP} - \frac{(\text{TP} + \text{FP})(\text{TP} + \text{FN})}{N}}{\text{TP} + \text{FP} + \text{FN} - \frac{(\text{TP} + \text{FP})(\text{TP} + \text{FN})}{N}} \quad (9)$$

$$\text{F}_1 = \frac{2 \text{TP}}{2 \text{TP} + \text{FP} + \text{FN}} \quad (10)$$

A light-weight postprocessing routine is applied: for every pixel the average of the mask values inside a 3×11 window (3 km wide, 0.7 km tall) is computed. If that local mean exceeds the cross-validated threshold $n = 0.05$, the pixel is flagged as convective; otherwise it is labelled as stratiform, to return a discrete representation in which each pixel has been assigned a value of either 0 or 1 (or NaN). After thresholding, a 2×2 confusion matrix with **true positives** (TP), **false positives** (FP), **false negatives** (FN), and **true negatives** (TN) is obtained. All four metrics above are built from these counts.

4. Case Studies

The performance of the model is illustrated through three case studies.

Fig. 7 presents a 500 km slice through the simulated Hurricane Milton, capturing a broad stratiform shield with embedded convection between approximately 150 km and 320 km along-track. The brightness temperature field (upper-left panel) exhibits sharp drops only in narrow bands, suggesting the presence of isolated deep convective towers embedded within an otherwise extensive anvil. This structure is corroborated by the reflectivity panel (centre-left), which reveals a broad layer of 0–15 dBZ reflectivities spanning altitudes of 6–15 km. The Doppler velocity panel (bottom-left) displays a characteristically noisy pattern, yet clear upward motion signatures (yellow–red) can still be identified near the convective tower cores. The C/S mask (middle-right) translates these dynamical indicators into a continuous convective index, which peaks at unity in regions where $|w| > 3$ m/s.

The U-Net reconstruction (bottom-right) captures both the location and vertical extent of these convective cores with high fidelity. Notably, the major updraughts between 180–200 km and 240–270 km are recovered with near pixel-perfect accuracy. Some minor discrepancies remain, however, as the network exhibits a slight over-dilation of the convective areas.

Fig. 8 illustrates the result of transforming the soft convection index into a binary classification field. The impact of this operation is evident in the upper-left panel: fine filaments visible in the raw mask (see Fig. 7) are eliminated, while the principal convective core is consolidated into a solid, contiguous structure. Applying the same thresholding process to the U-Net output (upper-right panel) yields a similarly coherent reconstruction.

The lower panel combines the two post-processed masks into a four-colour confusion map. True positives (red) dominate the convective core, indicating that the network not only identifies the convective region correctly but also captures its full vertical extent. True negatives (blue) are prevalent across the stratiform canopy, confirming that the model exhibits a low false alarm rate. Most classification errors manifest as a narrow yellow halo of false positives surrounding the edges of the convective towers. False negatives (green) are absent in this particular example and were observed only rarely across the entire test set.

Fig. 9 presents case study #2, which features a more fragmented convective structure compared to case study #1. The scene includes a chain of convective bursts embedded within a broad stratiform shield. The brightness temperature trace (upper-left panel) shows repeated dips between 130 km

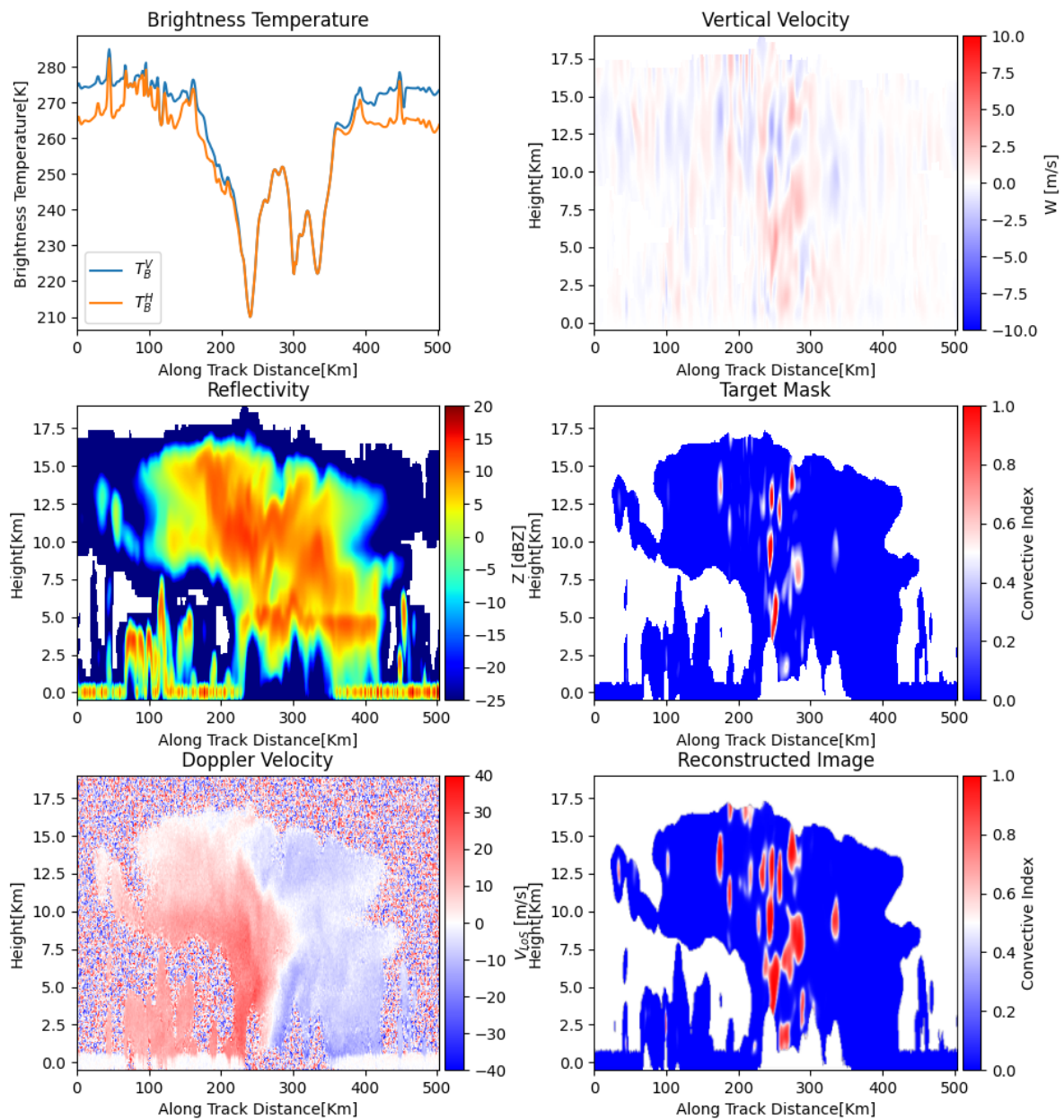


Figure 7. Case study #1 with input data (left column) and output (right column) for the CONSTRAINN-Large network. Top-left: Brightness temperatures, Center-left: Reflectivity, Bottom-left: Doppler velocity, Top-right: Raw wind vertical velocity, Center-right: Target Mask, Bottom-right: reconstructed image.

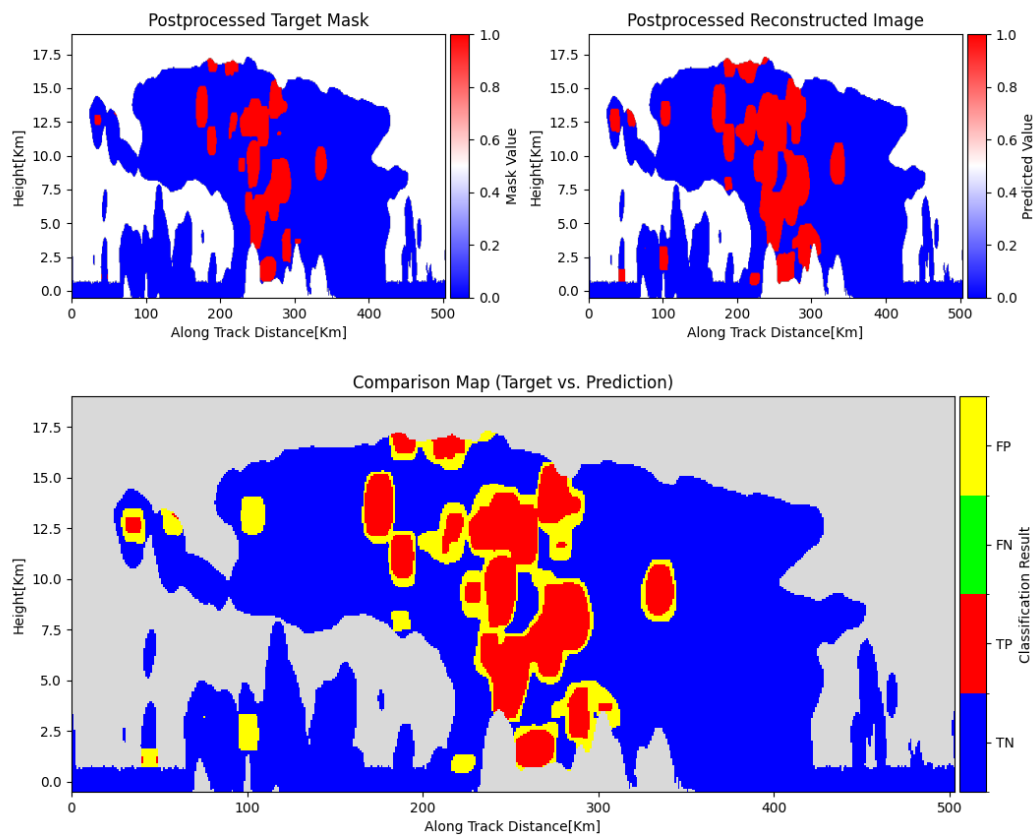


Figure 8. Binary thresholded output from the same sample of Fig. 7. Top-left: Postprocessed C/S Mask. Top-right: Postprocessed reconstructed image, Bottom: Overlapped images, highlighting True Positive, True Negative, False Positive and False Negatives regions.

and 320 km, indicating the presence of multiple overshooting tops rather than a single, well-defined eyewall. The reflectivity field confirms this pattern, revealing narrow columns exceeding 15 dBZ embedded within an expansive 5–15 dBZ stratiform layer, which deepens from around 5 km on the left to over 15 km at 400 km along-track.

The Doppler velocity panel displays corresponding streaks of intense upward motion (yellow–red), flanked by weaker downdraughts—typical signatures of pulse-type convection. The C/S mask successfully isolates the convective cores, assigning the surrounding ice clouds to the stratiform category. The U-Net reconstruction accurately retrieves all major convective cores and even captures the wispy overshooting feature near 150 km. However, it also introduces several small “satellite” blobs that remain below the threshold in the ground truth.

After applying the sliding-window post-processing filter (Fig. 10, top row), the predicted convective canopy appears smoother, and many of the spurious speckles disappear. The confusion map (bottom row) shows large true-positive regions (red) along the main convective towers, reflecting excellent recall. False positives (yellow) tend to appear around tower flanks and some mid-level anvil regions, while false negatives (green) are concentrated in a few narrow vertical spires—suggesting the model occasionally underestimates the extent of very slender cores. Nevertheless, the prevalence of true positives and true negatives across the scene confirms that overall precision remains high, despite the scene’s structural complexity.

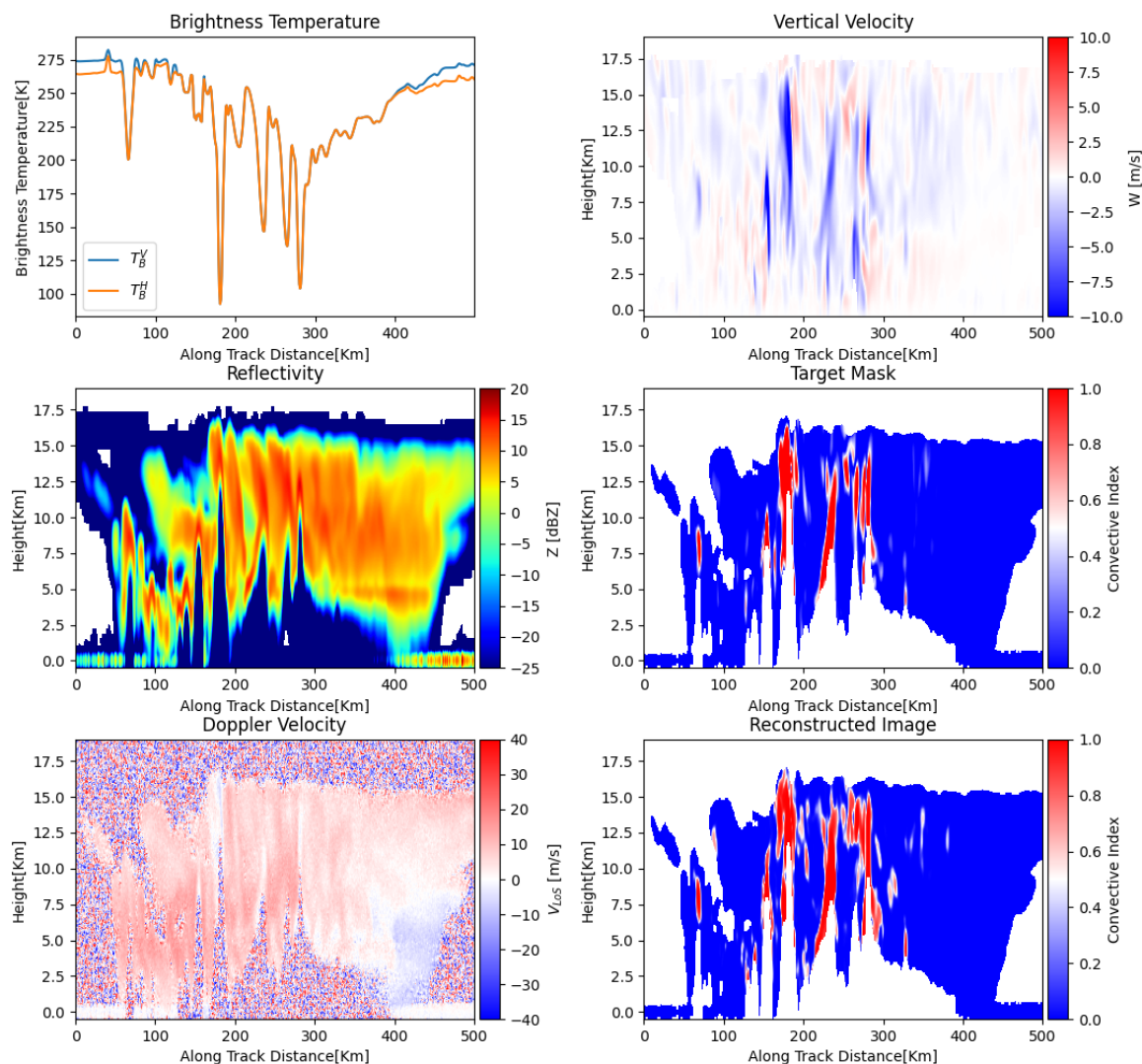


Figure 9. Case study #2 with input data (left column) and output (right column) for the CONSTRAINN-Large network. Top-left: Brightness temperatures, Center-left: Reflectivity, Bottom-left: Doppler velocity, Top-right: Raw wind vertical velocity, Center-right: Target Mask, Bottom-right: reconstructed image.

Finally, Figure 11 presents an additional case (case study #3), sampling a broad stratiform shield interrupted by a single intense convective tower, in contrast to the chain of smaller cells seen in previous cases. The brightness temperature panel reveals a sharp, V-shaped plunge of nearly 200 K centred around 70 km along-track. The reflectivity field confirms the presence of a narrow convective column extending above 17 km, with significant attenuation beneath it. The Doppler velocity panel supports this scenario, displaying a distinct needle-like vertical structure at the same location.

The U-Net reconstruction accurately predicts both the along-track position and the vertical extent of the core, while correctly identifying the downwind anvil as stratiform. Minor artefacts appear as faint streaks above 14 km, likely reflecting overconfident predictions of weaker convective activity. After post-processing, the filtered output maps are visually almost indistinguishable; however, the confusion image reveals subtle differences. The convective column is classified almost entirely as true positive (red). A thin halo of false positives (yellow) surrounds the top of the tower, indicating that the network is slightly more inclusive than the ground truth in classifying the anvil fringe. False negatives (green) are absent in this case.

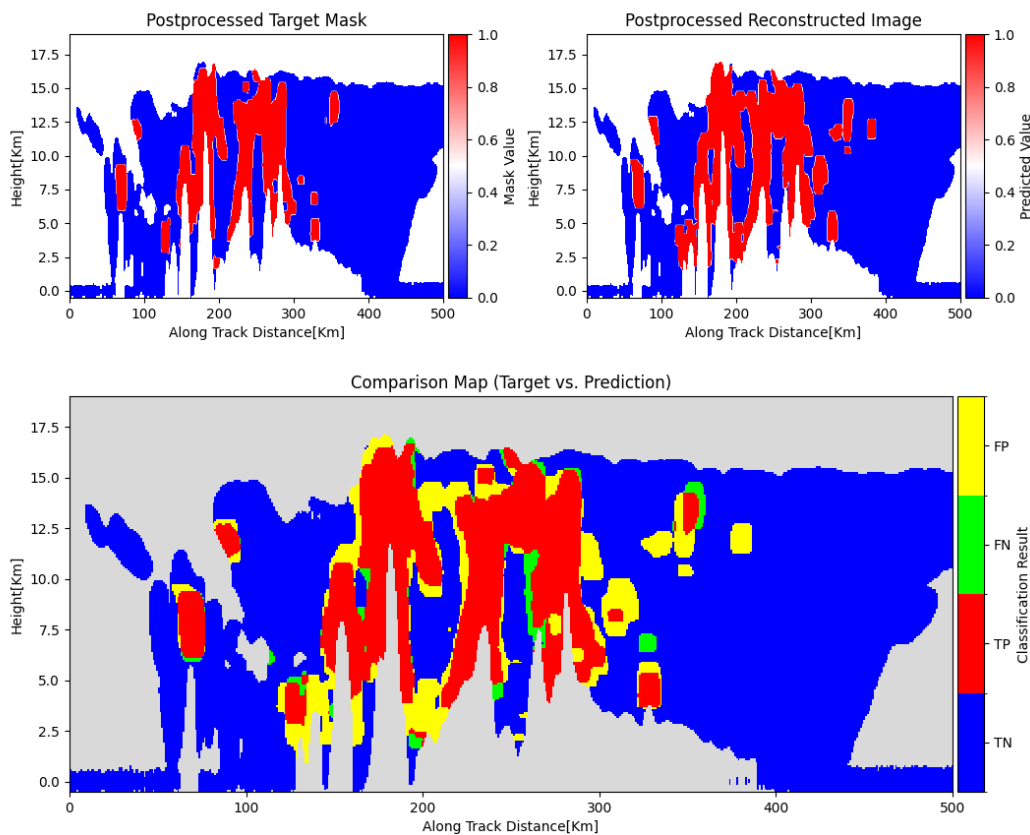


Figure 10. Binary thresholded output from the same sample of Fig. 9. Top-left: Postprocessed C/S Mask. Top-right: Postprocessed reconstructed image, Bottom: Overlapped images, highlighting True Positive, True Negative, False Positive and False Negatives regions

Overall, the three case studies demonstrate the strong performance of the U-Net architecture in C/S classification, effectively handling both isolated and embedded convection scenarios.

5. Results and Discussion

Table 2 returns a complete picture accounting for both the capacity-vs-skill curve and the contribution of each input channel. Moving from *Mini* to *Medium* and then to *Large* trims the pixel-wise losses almost monotonically (BCE from 0.031 \rightarrow 0.028 \rightarrow 0.023; MAE from 0.0153 \rightarrow 0.0133 \rightarrow 0.0098) and lifts ETS from 0.481 to 0.553, while FAR drops by roughly four percentage points overall. The returns, however, diminish: the medium model spends 4 \times the parameters of the mini version for a 10–12 % gain in the continuous metrics, whereas the large model costs an order of magnitude more parameters but only a further 15–20 % improvement. In practice, therefore, the medium configuration may offer the best cost–benefit ratio for an operational setting, with the large model acting as a high-skill but GPU-hungry benchmark, especially training-wise.

The channel ablations rows (from 4th to 8th) refine this picture. Removing either brightness temperature or Doppler velocity perturbs all scores by less than half a percent, evidence that the network can largely substitute one signal with the other two. Dropping reflectivity is more nuanced: the continuous losses improve slightly and FAR plunges to 0.188, but POD falls to 0.944 as the network

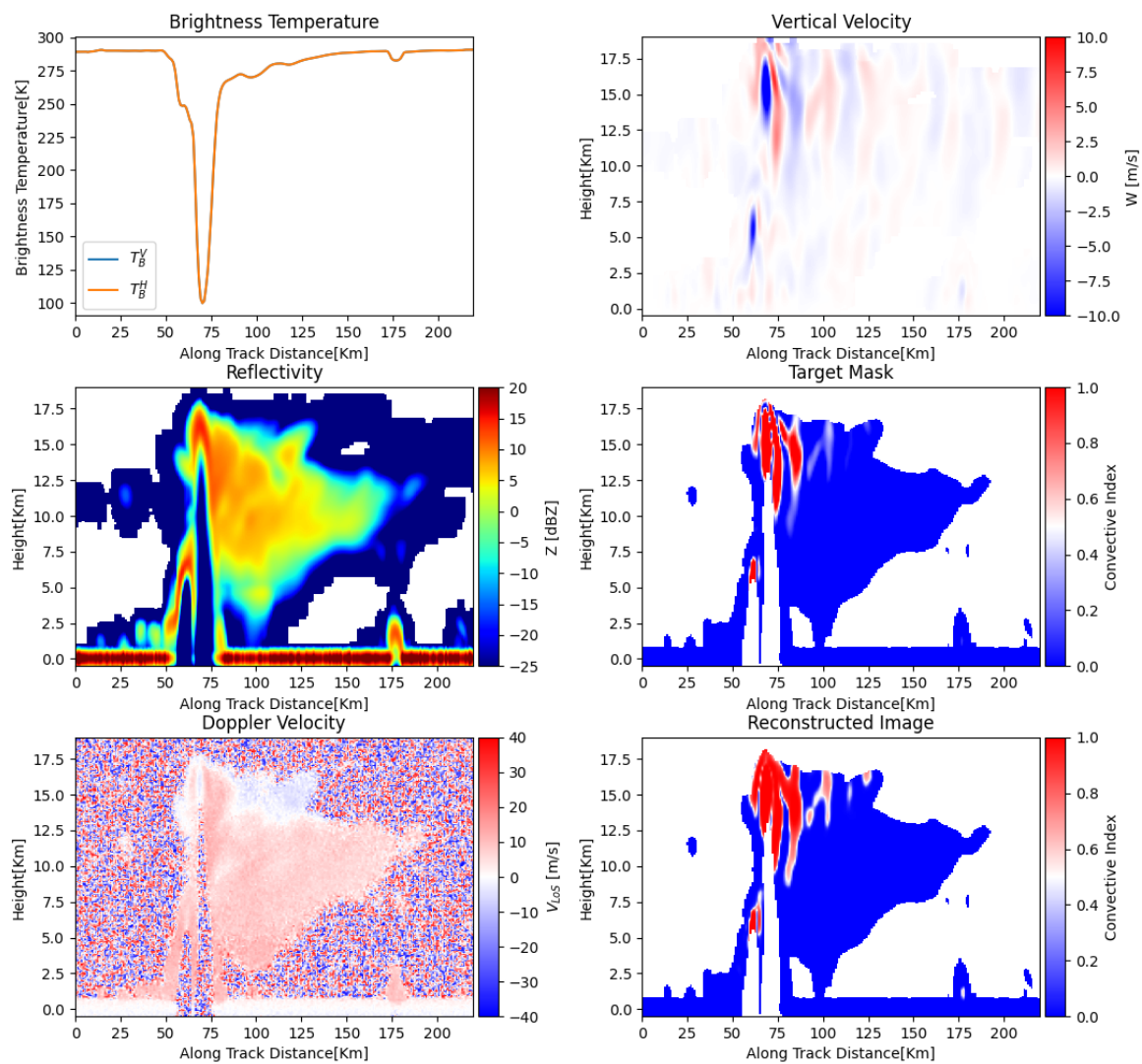


Figure 11. Case study #3 with input data (left column) and output (right column) for the CONSTRAINN-Large network. Top-left: Brightness temperatures, Center-left: Reflectivity, Bottom-left: Doppler velocity, Top-right: Raw wind vertical velocity, Center-right: Target Mask, Bottom-right: reconstructed image.

misses more weak convective examples, indicating that reflectivity adds recall at the expense of extra noise along core edges. The single-channel experiments underline Doppler's importance: a model driven only by Doppler velocity scores the highest ETS (0.604) and lowest FAR (0.185), yet its POD slips to 0.961, confirming that velocity alone captures vertical-motion structure but sometimes underrates marginal convection. Relying solely on reflectivity performs almost on par with the full model in POD but lags behind in every other metric, reinforcing the view that the three sensors are synergistic, with Doppler providing the bulk of structural skill and reflectivity acting as a recall booster.

6. Conclusions

This study introduces CONSTRAINN, a family of U-Net models trained on simulated data replicating the expected measurements from the WIVERN mission, to deliver a continuous, physically interpretable index of convective activity. By converting simulated vertical winds into a continuous convective/stratiform mask and by fusing Doppler velocity, reflectivity and brightness temperature information, the approach offers a reliable methodology to estimate vertical wind speed, as required

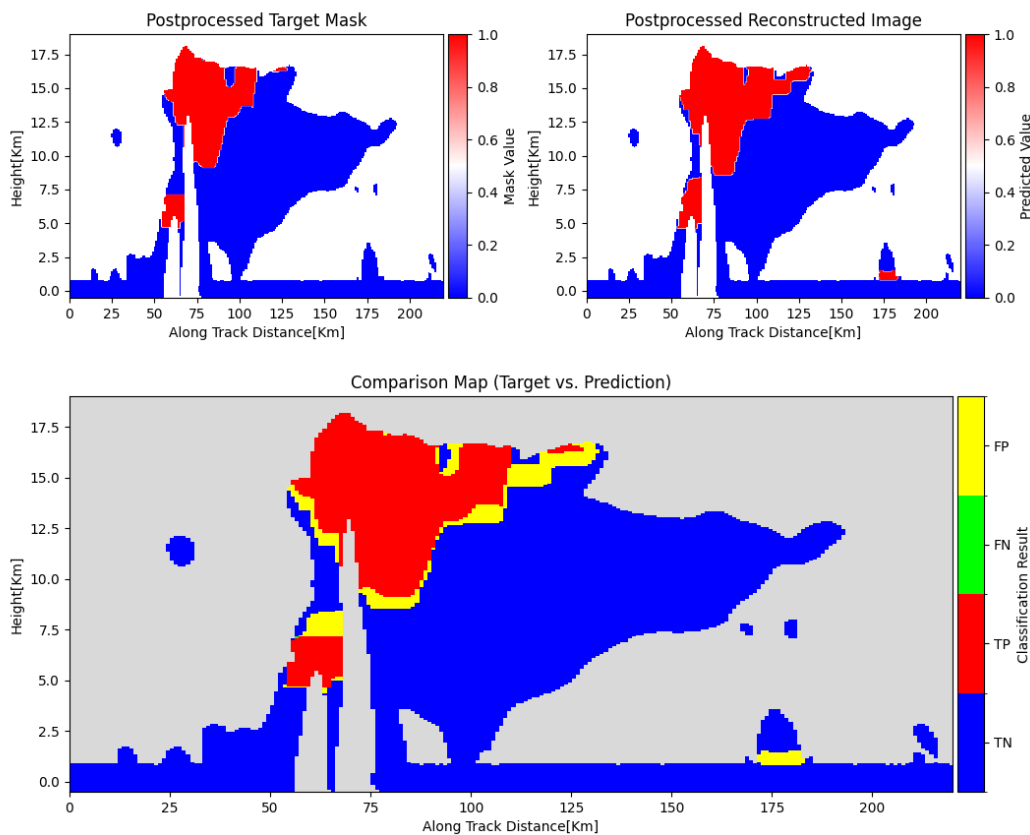


Figure 12. Binary thresholded output from the same sample of Fig. 11. Top-left: Postprocessed C/S Mask. Top-right: Postprocessed reconstructed image, Bottom: Overlapped images, highlighting True Positive, True Negative, False Positive and False Negatives regions

by the mission’s Level-2 retrieval chain. On the hurricane Milton benchmark a mean squared error of 0.38% is achieved, with an ETS of 60%, a POD of 98% and a FAR of 18%. It is worth noticing that, given that the convective pixels exceeding 1 m/s make up about 3.6% of our data, this FAR mostly reflects the network dilating real convection cores by a few pixels rather than fabricating artificial convective regions, an error that is considered acceptable within our application domain.

The current models are hurricane-focused and do not distinguish between downdrafts and updrafts. Future works might include generalization of the presented models to retrieve directly the vertical wind velocity, preserving the direction of movement. Moving toward a wider range of applicable scenarios, a natural improvement and future work should consist in generalizing the model architecture to different observational scenarios, such as mid-latitude systems, meso-scale convective systems, frontal systems or polar lows. Porting the same architecture to EarthCARE data, INCUS and other upcoming Doppler missions would further consolidate a unified, convection classifier for the next generation of space-borne atmospheric radars.

Author Contributions: AB wrote part of the paper, defined and supervised the project. F. Mustich drafted the paper, built the U-NET, and did the data analysis. F. Manconi built the training dataset and contributed to Sect. 2.1. AP run the WRF simulations. PK reviewed the paper and contributed to Sect. 3.

Model	BCE↓	MAE↓	MSE↓	ETS↑	FAR↓	POD↑	F ₁ ↑
CONSTRAINN-Mini	0.0311	0.0153	0.0066	0.481	0.253	0.978	0.815
CONSTRAINN-Medium	0.0281	0.0133	0.0057	0.512	0.238	0.982	0.829
CONSTRAINN-Large	0.0230	0.0098	0.0042	0.553	0.217	0.983	0.845
CONSTRAINN-Large (No Br. Temperature)	0.0238	0.0104	0.0044	0.547	0.220	0.980	0.842
CONSTRAINN-Large (No Doppler Velocity)	0.0243	0.0106	0.0046	0.548	0.220	0.984	0.844
CONSTRAINN-Large (No Reflectivity)	0.0238	0.0089	0.0038	0.580	0.188	0.944	0.855
CONSTRAINN-Large (Only Doppler Velocity)	0.0240	0.0098	0.0042	0.604	0.185	0.961	0.865
CONSTRAINN-Large (Only Reflectivity)	0.0248	0.0110	0.0048	0.543	0.222	0.981	0.841

Table 2. Validation performance of the three CONSTRAINN variants. Arrows indicate whether lower (↓) or higher (↑) values are better.

Funding: This research has been supported by the European Space Agency under the activities “WInd VELOCITY Radar Nephoscope (WIVERN) Phase A Science and Requirements Consolidation Study” (ESA Contract Number RFP/3-18420/24/NL/IB/ab). This study was carried out within the Space It Up project funded by the Italian Space Agency (ASI) and the Ministry of University and Research (MUR) under contract no. 2024-5-E.0 – CUP no. I53D2400060005.

Acknowledgments: This research used the Felipe High Performance Computing Facility at the Politecnico di Torino. Computational resources were also provided by HPC@POLITO, a project of Academic Computing within the Department of Control and Computer Engineering at the Politecnico di Torino (<http://hpc.polito.it>)

Conflicts of Interest: The authors declare no conflict of interest. The funders had no role in the design of the study; in the collection, analyses, or interpretation of data; in the writing of the manuscript, or in the decision to publish the results.

References

- Illingworth, A.J.; Battaglia, A.; Bradford, J.; Forsythe, M.; Joe, P.; Kollias, P.; Lean, K.; Lori, M.; Mahfouf, J.F.; Melo, S.; Midthassel, R.; Munro, Y.; Nicol, J.; Potthast, R.; Rennie, M.; Stein, T.H.M.; Tanelli, S.; Tridon, F.; Walden, C.J.; Wolde, M. WIVERN: A New Satellite Concept to Provide Global In-Cloud Winds, Precipitation, and Cloud Properties. *Bull. Amer. Met. Soc.* **2018**, *99*, 1669–1687, [<https://doi.org/10.1175/BAMS-D-16-0047.1>]. doi:10.1175/BAMS-D-16-0047.1.
- Battaglia, A.; Rizik, A.; Sikaneta, I.; Tridon, F. I and Qs Simulation and Processing Envisaged for Spaceborne Polarization Diversity Doppler Radars. *IEEE Trans. Geosci. Remote Sens.* **2025**, *63*, 1–14. doi:10.1109/TGRS.2025.3529672.
- ESA WIVERN Team. Report for Mission Selection: Earth Explorer 11 Candidate Mission WIVERN, European Space Agency, Noordwijk, The Netherlands. Technical report, ESA-EOPSM-WIVE-RP-4798, 2025. DOI: 10.5281/zenodo.15607041.
- Sasso, N.; Borderies, M.; Chambon, P.; others. Impact of WIVERN wind observations on Arpege Numerical Weather Prediction model forecasts using an Ensemble of Data Assimilation method. *Quarterly Journal of the Royal Meteorological Society* **2025**. doi:10.1002/qj.4991.
- Federico, S.; Torcasio, R.C.; Transerici, C.; Montopoli, M.; Cambiotti, C.; Manconi, F.; Battaglia, A.; Pourshams, M. Assimilating WIVERN winds in WRF model: an application to the outstanding case of the Medicane Ianos. *Atm. Meas. Tech.* **2025**. submitted, doi:XXXXX.
- Battaglia, A.; ; Cambiotti, C.; Carbone, A.F.; Da Silva, S. Reconstruction of the Horizontal Wind Field Inside Weather Systems from the Sparse Sampling Envisaged for the Wind Velocity Radar Nephoscope (WIVERN) Mission. IGARSS 2024 - 2024 IEEE International Geoscience and Remote Sensing Symposium, 2024, pp. 8925–8927. doi:10.1109/IGARSS53475.2024.10640420.
- Da Silva, S.; Battaglia, A.; Cambiotti, C.; Carbone, A.F. Sparse sampling reconstruction of wind fields for space-borne Doppler radars. *IEEE Trans. Geosci. Remote Sens.* **2025**. submitted, doi:XXXXX.
- Tridon, F.; Battaglia, A.; Rizik, A.; Scarsi, F.E.; Illingworth, A. Filling the Gap of Wind Observations Inside Tropical Cyclones. *Earth and Space Science* **2023**, *10*, e2023EA003099, [<https://agupubs.onlinelibrary.wiley.com/doi/pdf/10.1029/2023EA003099>]. e2023EA003099, doi:<https://doi.org/10.1029/2023EA003099>.

9. Schumacher, C.; Funk, A. Assessing Convective-Stratiform Precipitation Regimes in the Tropics and Extratropics With the GPM Satellite Radar. *Geophysical Research Letters* **2023**, *50*, e2023GL102786, [<https://agupubs.onlinelibrary.wiley.com/doi/pdf/10.1029/2023GL102786>]. e2023GL102786 2023GL102786, doi:<https://doi.org/10.1029/2023GL102786>.
10. Battaglia, A.; Kollias, P.; Dhillon, R.; Roy, R.; Tanelli, S.; Lamer, K.; Grecu, M.; Lebsock, M.; Watters, D.; Mroz, K.; Heymsfield, G.; Li, L.; Furukawa, K. Spaceborne Cloud and Precipitation Radars: Status, Challenges, and Ways Forward. *Reviews of Geophysics* **2020**, *58*, e2019RG000686, [<https://agupubs.onlinelibrary.wiley.com/doi/pdf/10.1029/2019RG000686>]. e2019RG000686 10.1029/2019RG000686, doi:10.1029/2019RG000686.
11. Houze Jr., R.A.; Rasmussen, K.L.; Zuluaga, M.D.; Brodzik, S.R. The variable nature of convection in the tropics and subtropics: A legacy of 16 years of the Tropical Rainfall Measuring Mission satellite. *Reviews of Geophysics* **2015**, *53*, 994–1021, [<https://agupubs.onlinelibrary.wiley.com/doi/pdf/10.1002/2015RG000488>]. doi:10.1002/2015RG000488.
12. Mroz, K.; Battaglia, A.; Lang, T.J.; Cecil, D.J.; Tanelli, S.; Tridon, F. Hail-Detection Algorithm for the GPM Core Observatory Satellite Sensors. *J. Appl. Meteorol. Climatol.* **2017**, *56*, 1939–1957, [<https://doi.org/10.1175/JAMC-D-16-0368.1>]. doi:10.1175/JAMC-D-16-0368.1.
13. Kollias, P.; Albrecht, B.A.; Marks, F. Why Mie? *Bulletin of the American Meteorological Society* **2002**, *83*, doi:10.1175/bams-83-10-1471(2002)083<1471:wm>2.3.co;2.
14. Kollias, P.; Szyrmer, W.; Zawadzki, I.; Joe, P. Considerations for spaceborne 94 GHz radar observations of precipitation. *Geophys. Res. Lett.* **2007**, *34*, [<https://agupubs.onlinelibrary.wiley.com/doi/pdf/10.1029/2007GL031536>]. doi:10.1029/2007GL031536.
15. Haynes, J.M.; L'Ecuyer, T.S.; Stephens, G.L.; Miller, S.D.; Mitrescu, C.; Wood, N.B.; Tanelli, S. Rainfall retrieval over the ocean with spaceborne W-band radar. *Journal of Geophysical Research Atmospheres* **2009**, *114*, doi:10.1029/2008JD009973.
16. Battaglia, A.; Tanelli, S.; Kobayashi, S.; Zrnica, D.; Hogan, R.J.; Simmer, C. Multiple-scattering in radar systems: A review. *J. Quant. Spectrosc. Radiat. Transfer* **2010**, *111*, 917 – 947. doi:<https://doi.org/10.1016/j.jqsrt.2009.11.024>.
17. Stephens, G.; Polcher, J.; Zeng, X.; van Oevelen, P.; Poveda, G.; Bosilovich, M.; Ahn, M.H.; Balsamo, G.; Duan, Q.; Hegerl, G.; Jakob, C.; Lamptey, B.; Leung, R.; Piles, M.; Su, Z.; Dirmeyer, P.; Findell, K.L.; Verhoef, A.; Ek, M.; L'Ecuyer, T.; Roca, R.; Nazemi, A.; Dominguez, F.; Klocke, D.; Bony, S. The First 30 Years of GEWEX. *Bulletin of the American Meteorological Society* **2023**, *104*, E126 – E157. doi:10.1175/BAMS-D-22-0061.1.
18. Takahashi, H.; Luo, Z.J.; Stephens, G.L. Level of neutral buoyancy, deep convective outflow, and convective core: New perspectives based on 5 years of CloudSat data. *Journal of Geophysical Research* **2017**, *122*, doi:10.1002/2016JD025969.
19. Steiner, M.; Houze, R.; Yuter, S. Climatological characterization of three-dimensional storm structure from operational radar and rain gauge data. *Journal of Applied Meteorology* **1995**, *34*, 1978–2007. doi:10.1175/1520-0450(1995)034<1978:CCOTDS>2.0.CO;2.
20. Yang, Y.; Chen, X.; Qi, Y. Classification of convective/stratiform echoes in radar reflectivity observations using a fuzzy logic algorithm. *Journal of Geophysical Research: Atmospheres* **2013**, *118*, 1896–1905, [<https://agupubs.onlinelibrary.wiley.com/doi/pdf/10.1002/jgrd.50214>]. doi:<https://doi.org/10.1002/jgrd.50214>.
21. Yang, Z.; Liu, P.; Yang, Y. Convective/Stratiform Precipitation Classification Using Ground-Based Doppler Radar Data Based on the K-Nearest Neighbor Algorithm. *Remote Sensing* **2019**, *11*, doi:10.3390/rs11192277.
22. Cintineo, J.L.; Pavolonis, M.J.; Sieglaff, J.M.; Wimmers, A.; Brunner, J.; Bellon, W. A deep-learning model for automated detection of intense midlatitude convection using geostationary satellite images. *Weather and Forecasting* **2020**, *35*, 2567–2588.
23. Lee, Y.; Kummerow, C.D.; Ebert-Uphoff, I. Applying machine learning methods to detect convection using Geostationary Operational Environmental Satellite-16 (GOES-16) advanced baseline imager (ABI) data. *Atmospheric Measurement Techniques* **2021**, *14*, 2699–2716. doi:10.5194/amt-14-2699-2021.
24. Das, S.; Wang, Y.; Gong, J.; Ding, L.; Munchak, S.J.; Wang, C.; Wu, D.L.; Liao, L.; Olson, W.S.; Barahona, D.O. A Comprehensive Machine Learning Study to Classify Precipitation Type over Land from Global

- Precipitation Measurement Microwave Imager (GPM-GMI) Measurements. *Remote Sensing* **2022**, *14*. doi:10.3390/rs14153631.
25. Orescanin, M.; Petković, V.; Powell, S.W.; Marsh, B.R.; Heslin, S.C. Bayesian deep learning for passive microwave precipitation type detection. *IEEE Geoscience and Remote Sensing Letters* **2021**, *19*, 1–5.
 26. Hoeller, J.; Fiévet, R.; Engelbrecht, E.; Haerter, J.O. U-Net Segmentation for the Detection of Convective Cold Pools From Cloud and Rainfall Fields. *Journal of Geophysical Research: Atmospheres* **2024**, *129*, e2023JD040126, [<https://agupubs.onlinelibrary.wiley.com/doi/pdf/10.1029/2023JD040126>]. e2023JD040126 2023JD040126, doi:<https://doi.org/10.1029/2023JD040126>.
 27. Han, L.; Liang, H.; Chen, H.; Zhang, W.; Ge, Y. Convective Precipitation Nowcasting Using U-Net Model. *IEEE Transactions on Geoscience and Remote Sensing* **2022**, *60*, 1–8. doi:10.1109/TGRS.2021.3100847.
 28. Zhang, J.; He, M. Methodology for Severe Convective Cloud Identification Using Lightweight Neural Network Model Ensembling. *Remote Sensing* **2024**, *16*. doi:10.3390/rs16122070.
 29. Deng, M.; Han, Y.; Liu, Y.; Dong, L.; Zhou, Q.; Zhang, Y.; Deng, X.; Lu, T. Development of a Novel One-Dimensional Nested U-Net Cloud-Classification Model (1D-CloudNet). *Remote Sensing* **2025**, *17*. doi:10.3390/rs17030519.
 30. Ramos, L.T.; Sappa, A.D. Leveraging U-Net and selective feature extraction for land cover classification using remote sensing imagery. *Scientific Reports* **2025**, *15*, 784.
 31. Yan, C.; Fan, X.; Fan, J.; Wang, N. Improved U-Net Remote Sensing Classification Algorithm Based on Multi-Feature Fusion Perception. *Remote Sensing* **2022**, *14*. doi:10.3390/rs14051118.
 32. Meza, J.; Anderson, N.; Tsultrim, T. Weather-Forecasting UNET: Leveraging a U-Net Architecture for Probabilistic Tornado Prediction from Multivariate Reanalysis Data **2024**. *60*, 1–8.
 33. Rizik, A.; Battaglia, A.; Tridon, F.; Scarsi, F.; Kötsche, A.; Kalesse-Los, H.; Maahn, M.; Illingworth, A. Impact of cross-talk on reflectivity and Doppler measurements for the WIVERN Polarization Diversity Doppler Radar. *IEEE Trans. Geosci. Remote Sens.* **2023**.
 34. Manconi, F.; Martire, P.; Stesina, F.; Battaglia, A. High accuracy attitude determination of a spacecraft with a fast-rotating Doppler radar reflector. *Acta Astronautica* **2025**, *233*, 66–81. doi:<https://doi.org/10.1016/j.actaastro.2025.03.026>.
 35. Battaglia, A.; Martire, P.; Caubet, E.; Phalippou, L.; Stesina, F.; Kollias, P.; Illingworth, A. Observation error analysis for the WInd VELOCITY Radar Nephoscope W-band Doppler conically scanning spaceborne radar via end-to-end simulations. *Atmospheric Measurement Techniques* **2022**, *15*. doi:10.5194/amt-15-3011-2022.
 36. Fabry, F. *Radar Meteorology: Principles and Practice*; Cambridge University Press, 2015. doi:10.1017/CBO9781107707405.
 37. Stephens, G.L.; Kummerow, C.D. The Remote Sensing of Clouds and Precipitation from Space: A Review. *J. Atmos. Sci.* **2007**, *64*, 3742–3765. doi: <http://dx.doi.org/10.1175/2006JAS2375.1>.
 38. Luo, Z.; Stephens, G.L.; Emanuel, K.A.; Vane, D.G.; Tourville, N.; Haynes, J. On the Use of CloudSat and data for estimating Hurricane Intensity. *IEEE Geosci. Remote Sens. Lett.* **2008**, *5*, 13–16.
 39. Matrosov, S.Y. Potential for attenuation-based estimations of rainfall rate from CloudSat. *Geophysical Research Letters* **2007**, *34*. doi:10.1029/2006GL029161.
 40. Heymsfield, G.M.; Tian, L.; Heymsfield, A.J.; Li, L.; Guimond, S. Characteristics of Deep Tropical and Subtropical Convection from Nadir-Viewing High-Altitude Airborne Doppler Radar. *Journal of the Atmospheric Sciences* **2010**, *67*, 285 – 308. doi:10.1175/2009JAS3132.1.
 41. Galfione, A.; Battaglia, A.; Puigdomènech Treserras, B.; Kollias, P. First insights into deep convection by the Doppler velocity measurements of the EarthCARE’s Cloud Profiling Radar. *EGU Sphere* **2025**, *2025*, 1–25. doi:10.5194/egusphere-2025-1914.
 42. Spencer, R.W.; Howland, M.R.; Santek, D.A. Severe Storm Identification with Satellite Microwave Radiometry: An Initial Investigation with Nimbus-7 SMMR Data. *J. Appl. Meteorol. Climatol.* **1987**, *26*, 749 – 754. doi:10.1175/1520-0450(1987)026<0749:SSIWSM>2.0.CO;2.
 43. Hong, Y.; Kummerow, C.D.; Olson, W.S. Separation of Convective and Stratiform Precipitation Using Microwave Brightness Temperature. *J. Appl. Meteorol.* **1999**, *38*, 1195 – 1213. doi:10.1175/1520-0450(1999)038<1195:SOCASP>2.0.CO;2.
 44. Battaglia, A.; Mroz, K.; Lang, T.; Tridon, F.; Tanelli, S.; Tian, L.; Heymsfield, G.M. Using a multiwavelength suite of microwave instruments to investigate the microphysical

- structure of deep convective cores. *J. Geophys. Res. Atm.* **2016**, *121*, 9356–9381, [<https://agupubs.onlinelibrary.wiley.com/doi/pdf/10.1002/2016JD025269>]. doi:10.1002/2016JD025269.
45. Leppert, K.D.; Cecil, D.J. Signatures of Hydrometeor Species from Airborne Passive Microwave Data for Frequencies 10–183 GHz. *J. Appl. Meteorol. Climatol.* **2015**, *54*, 1313–1334. doi: <http://dx.doi.org/10.1175/JAMC-D-14-0145>.
46. Battaglia, A.; Mroz, K.; Cecil, D. Chapter 9 - Satellite hail detection. In *Precipitation Science*; Michaelides, S., Ed.; Elsevier, 2022; pp. 257–286. doi: <https://doi.org/10.1016/B978-0-12-822973-6.00006-8>.
47. Battaglia, A.; Panegrossi, G. What Can We Learn from the CloudSat Radiometric Mode Observations of Snowfall over the Ice-Free Ocean? *Remote Sensing* **2020**, *12*. doi:10.3390/rs12203285.



© 2020 by the authors. Licensee MDPI, Basel, Switzerland. This article is an open access article distributed under the terms and conditions of the Creative Commons Attribution (CC BY) license (<http://creativecommons.org/licenses/by/4.0/>).